Additive Manufacturing, Vol. 41, (2021, May): 101966. DOI.

Additive Manufacturing and Mechanical Properties of the Dense and Crack Free Zr-Modified Aluminum Alloy 6061 Fabricated by the Laser-Powder Bed Fusion

Abhishek Mehta
Department of Materials Science and Engineering, University of Central Florida, Orlando, FL, USA
Le Zhou
Department of Materials Science and Engineering, University of Central Florida, Orlando, FL, USA
Thinh Huynh
Department of Materials Science and Engineering, University of Central Florida, Orlando, FL, USA
Sharon Park
Department of Materials Science and Engineering, University of Central Florida, Orlando, FL, USA
Holden Hyer
Department of Materials Science and Engineering, University of Central Florida, Orlando, FL, USA
Shutao Song

Department of Mechanical and Aerospace Engineering, University of Central Florida, Orlando, FL, USA
Yunali Bai
Department of Mechanical and Aerospace Engineering, University of Central Florida, Orlando, FL, USA
D. Devin Imholte
Nuclear Fuels and Materials Division, Idaho National Laboratory, Idaho Falls, ID, USA
Nicolas E. Woolstenhulme
Nuclear Fuels and Materials Division, Idaho National Laboratory, Idaho Falls, ID, USA
Daniel M. Wachs
Nuclear Fuels and Materials Division, Idaho National Laboratory, Idaho Falls, ID, USA
Yongho Sohn
Department of Materials Science and Engineering, University of Central Florida, Orlando, FL, USA

Abstract

For additive manufacturing such as laser powder bed fusion (LPBF), commercial aluminum alloy (AA) 6061 is typically considered unsuitable due to formation of solidification cracking and/or excessive porosity. In this study, to improve buildability/printability of AA6061, 1 wt% of Zr was alloyed to produce Zr-modified AA6061 by LPBF. Powders of unmodified and Zr-modified AA6061 were produced by gas atomization, and utilized as a feed-stock for the LPBF to fabricate specimens for microstructural examination and mechanical testing. The as-built unmodified AA6061 exhibited poor printability due to formation of cracks and porosity in the microstructure regardless of LPBF parameters. However, the Zr-modified AA6061 exhibited near full density, with substantial reduction in porosities without any solidification crack for a certain LPBF processing window. The improved printability of Zr-modified AA6061 was attributed to a significant grain refinement, which would reduce the solidification cracking susceptibility by hampering the epitaxial growth of long columnar cracks, as observed in unmodified AA6061. Yield strength, tensile strength and strain-at-failure for the as-built Zr-modified AA6061 were determined to be 210 MPa, 268 MPa, and 26.5%, respectively. These are superior to the tensile properties of AA6061 in O-annealed condition or in as-cast condition. After T6 heat treatment, yield strength, tensile strength and strain-at-failure of Zr-modified AA6061 were determined to be 300 MPa, 327 MPa, and 14%, which were again superior to the tensile properties of wrought AA6061 in T6 heat treated condition. Effects of Zr addition on the buildability/printability improvement and mechanical properties of AA6061 were corroborated by a variety of electron microscopic characterization.

Graphical Abstract

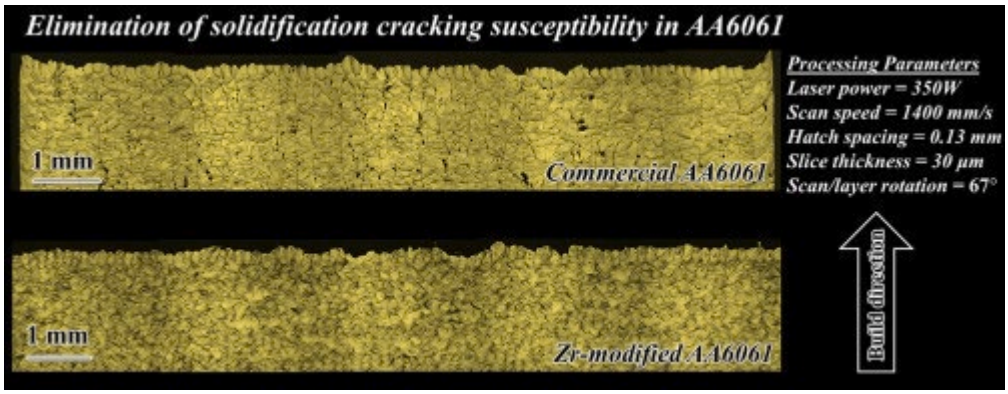

Keywords
Laser powder bed fusion, Aluminum alloy 6061, Zr-modification, Microstructure, Mechanical properties

1. Introduction
Aluminum alloy (AA) 6061 is used in a variety of engineering applications. For structural, automotive, and aerospace applications, T6 heat treated AA6061 alloys are used because of their high strength, good corrosion resistance, weldability, and machinability [1]. For nuclear applications, AA6061 is used as a cladding material to encapsulate various forms of fuel forms for research reactors including standard UAl_x, U_3O_8, and U_3Si_2 dispersion fuel meats currently in use as well as advanced Zr laminated U-10Mo fuel in monolithic fuel plates [2], [3], [4], [5], [6], [7], [8], [9]. These materials may have significant applications in emerging advanced reactors applications (e.g. micro-reactors). Presently, AA6061 is typically used mainly in wrought form, and it is not readily available for the powder bed fusion (PBF) additive manufacturing (AM) due to formation of excessive flaws such as pores and cracks. This poor printability can be linked to the large solidification range (~141 °C) [10], poor melt flowability, high thermal conductivity, high coefficient of thermal expansion, and large cracking susceptibility [11]. Native oxide layers may also adversely affect its printability [12]. As of today, AM of Al-alloys is limited to the alloys with near eutectic composition e.g. AlSi10Mg [13], [14], AlSi12 [15], [16], [17], AlSi7Mg0.3 (A356) [18], Al-10Ce [19] etc., which would exhibit good castability due to narrow solidification ranges and low hot tearing tendencies associated with low shrinkage of these alloys. However, these printable Al-alloys may not have the same application volume compared to other Al-alloys (e.g., 2xxx, 5xxx, 6xxx and 7xxx), which all suffer from the poor buildability/printability over a practical processing parametric range of laser PBF (LPBF) [20], [21], [22], [23].

Sonawane et al. [24] were first to investigate the cracking mechanism during LPBF processing of AA6061, and suggested that the solidification cracking in AA6061, propagating preferentially along the high angle grain, contributed towards the poor printability of AA6061. Several investigations [21], [25], [26], [27], [28], [29], [30] had examined the printability/buildability of AA6061 to reduce the solidification cracking susceptibility. These investigations were mainly focused on either minimizing the thermal gradient associated with LPBF to suppress the cracking associated with epitaxial grain growth or modify the alloy composition by the minor addition of the grain refiners to heterogeneously nucleate the fine grains which can better accommodate thermal and/or mechanical stresses associated with LPBF.
Loh *et* al. [25] were the first to characterize additively manufactured commercial AA6061 using LPBF by employing the Gaussian and uniform laser beam profiles and observed cracking in the as-built microstructure. Fulcher et al. [21] compared the as-built commercial AA6061 to AlSi10Mg, and suggested that solidification cracking tendency in AA6061 would be alleviated by either running a preheat scan or heating the build-plate. Similar approach was adopted by Uddin *et* al. [29], [31] who conducted the LPBF parametric optimization for commercial AA6061, and used the pre-heated build-plate (500 °C) to minimize the thermal gradient which substantially reduced the cracking. Maamoun *et* al. [30] also preheated the build plate to 200 °C to fabricated AA6061 samples, however, cracking was observed in the microstructure along with precipitation of nano-scale Si particles. Qbau *et* al. [28] added the 0.15 wt% Sc to commercial AA6061 and reported the complete elimination of cracking in Sc-modified AA6061. Similarly, Opprecht et al. [27] utilized YSZ coated AA6061 powders to eliminate cracking during LPBF fabrication, which was motivated by the work reported by Martin et al. [26], wherein they suggested to coated AA6061 powders with ZrH_2.

The challenge associated with LPBF of AA6061 brings an opportunity to improve the mechanical properties of AA6061, albeit modified with minor alloying additions, using unique microstructural development. Build plate heating may permanently modify the microstructure of AA6061 by excessive precipitation of Mg/Si-rich complex intermetallic, and may deplete Mg/Si from the matrix, which can be later utilized to form strengthening

precipitates (e.g. Mg_2Si after T6 heat treatment). Also, build plate heating sometimes does not result in complete elimination of cracking [30]. Addition of Sc is highly effective in eliminating the crack, however, it is 50–100 times more expensive than the alternative grain refiners (e.g., Zr examined in this study). Compositional modification by addition of compounds (e.g., ZrH_2 or YSZ) requires additional powder processing. Therefore, the main objective of this work is to investigate the effect of LPBF processing parameters on the printability of AA6061 alloy and subsequent improvement in printability through composition modification by a minor alloying addition. In this work, compositional modification was performed by adding 1.0 wt% Zr to commercial AA6061, denoted as *Zr-modified AA6061* hereafter in the manuscript. Powder feedstock of both unmodified and Zr-modified AA6061 were made by gas atomization. No additional powder surface modification was carried out and build plate temperature was kept at 100 °C. Microstructural characteristics of as-built alloys were examined for both unmodified and modified AA6061 to understand the effect of Zr on improved printability. The as-built, Zr-modified AA6061 was subjected to a two-step T6 heat treatment to assess the tensile properties before and after the heat treatment, and its enhanced mechanical behavior was corroborated with microstructural analyses.

2. Experimental details

2.1. Powder fabrication

Powder feedstock for LPBF were produced using pre-alloyed AA6061 charges. Modification of AA6061 alloy composition was carried out by mixing AA6061 with the Al–5 wt% Zr and Al–10 wt% Mg master alloys, with an aim of achieving 1 wt% Zr in AA6061 while maintaining the concentration of major alloying addition of Mg. Both unmodified AA6061 and Zr-modified AA6061 (i.e., AA6061 + 1 wt% Zr) powders were produced using close-coupled gas atomization system with double-induction melting furnaces. Both unmodified and Zr-modified AA6061 alloy compositions were melted between 950° and 1050 °C using graphite crucibles. Molten alloys were poured into a pre-heated (850–1000 °C) graphite crucible with a 2–2.5 mm diameter orifice. Atomization was performed with an Argon gas flow at a pressure of 2.5–3.0 MPa. Gas atomized powders were mechanically sieved and their size distribution was measured using Beckman Coulter LS^{TM} 13 320 laser diffraction particle size analyzer.

2.2. Laser powder bed fusion

Parametric investigation of unmodified and Zr-modified AA6061 alloys were carried out by LPBF, initially with 12 mm square cube samples, using SLM 125^{HL} (SLM Solutions Group AG, Lübeck, Germany). The cube samples were fabricated as functions of laser power and scan speed while keeping the slice thickness, hatch spacing, stripe pattern width and scan rotation constant. At a laser power of 200 W, samples were fabricated by varying the scan speed from 100 to 800 mm/s. At 350 W, cubes were fabricated by varying the scan speed from 400 to 1800 mm/s. Throughout the sample fabrication, slice thickness and hatch spacing were held constant at 0.03 mm and 0.13 mm, respectively. Stripe pattern width and scan rotation remained at 10 mm and 67°, respectively. Cube samples were built to ensure that the laser scan direction for the last melt pool was orthogonal to the one of the cube face, as shown in Fig. 1(a), for melt pool measurement. All cube samples were built on plate maintained at 100 °C, and in nitrogen gas with oxygen content below 0.2 wt%. Once the optimized LPBF parameters were identified for Zr-modified AA6061 without cracking, several tensile bars, as schematically shown in Fig. 1(b) were built parallel to the build plate (X-Y direction).

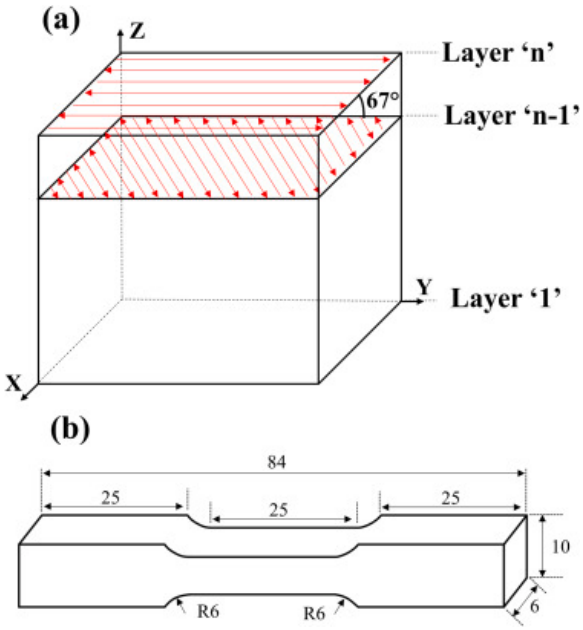

Fig. 1. Schematic representations of (a) layer rotation in a cube sample and (b) tensile bars built as per ASTM E8/E8M standard.

2.3. Heat treatment

Based on the cursory characterization and density measurements, the most dense sample produced (i.e. 1400 mm/s scan speed at 350 W laser power) was subjected to the subsequent heat treatment study to investigate the effect heat-treatment on the mechanical properties (i.e., hardness/tensile measurement). Traditional T6 heat treatment was carried out, wherein samples were initially solutionized at 500 °C for 1 h, and subsequently water-quenched. This temperature is also sufficient to precipitate supersaturated Al_3Zr precipitates, and simultaneously solutionize the other alloying elements. Then samples were subsequently heat treated at 160 °C for 10 h to artificially age and yield fine Mg_2Si precipitates.

2.4. Mechanical testing

Prior to the hardness measurement, all samples were metallographically polished down to 1 µm surface finish. Quasi-static nanoindentation testing was performed using a Hysitron™ TI Premier indenter with a Berkovich tip to document the mechanical behavior of the most dense LPBF specimen as a function of heat treatment steps. Oliver and Pharr's method [32], [33] was utilized to determine the Hardness (H) and Reduced Modulus (E_r) by analyzing the unloading part of the load displacement curve. Indentation testing was carried out at 5 mN peak load with 10 s of loading time, 3 s of holding at the peak load and 10 s of unloading.

Young's modulus (E) was estimated from the reduced modulus(E_r) using [32]:

(1)

$$\frac{1}{E_r} = \frac{1-\nu_s^2}{E} + \frac{1-\nu_i^2}{E_i}$$

where, E_i is the Young's modulus (1140 GPa) and ν_i is the Poisson's ratio (0.07) of the diamond indenter tip [34], and ν_s is the Poisson's ratio of the AA6061 (0.33). Hardness measurements were also carried out using Leco LV700 Vickers hardness tester at a load of 10 kgf and a dwell time of 10 s. For statistical consistency, minimum of twenty five indentations were carried out for nano-indentation and five indentations for Vickers hardness measurements for each sample.

Six tensile bars were fabricated using LPBF process with the dimensions in compliance to ASTM standards E8/E8M in the horizontal build orientation using the 350 W laser power traversing at 1400 mm/s. Fig. 1(b) shows the dimensions of the tensile bars fabricated using LPBF process. Three tensile bars were tested without any heat treatment (i.e., as-built), and three were tested after T6 heat treatment. All tensile bars were grounded down to 1200 grit to remove supports and to obtain the surface finish necessary for digital image correlation (DIC) measurements. DIC system consists of a Tokina AT-X Pro macro 100 mm−f/2.8−d lens with a resolution of 2448 × 2048 and VIC-2D 2009 software by Correlated Solutions, Inc. The tensile testing was carried out quasi-statically under uniaxial loading at room temperature using an MTS universal testing machine. For all tensile tests, quasi-static strain rate was maintained at 5×10^{-3} s^{-1} and strain was recorded using DIC system normal to the uniaxial loading direction at 1 Hz capture frequency. Then, DIC analysis was performed using a virtual extensometer for individual tensile bars to obtain the Engineering stress-strain curve using applied force on MTS machine.

2.5. Microstructural characterization

Prior to microstructural characterization, density measurements were performed on all cube samples to measure the amount of flaws, using both Archimedes principle and image analysis. All as-built cube surfaces were grounded to 600 grit to remove supports and to ensure surface homogeneity for density measurements via Archimedes' principle. Then, as-built samples were sectioned, along build direction (i.e., XZ cross-section) and normal to build direction (i.e., XY cross-section), and metallographically polished down to 0.05 µm surface finish. A minimum five optical micrographs were obtained at 50X magnification using Olympus LEXT OLS 3000 microscope for image analysis. Image analysis was performed using ImageJ (National Institutes of Health) to quantify the amount of flaws (i.e. cracks, porosity and lack-of-fusion flaws) observed on the metallographically polished cross-sections. By assuming that the flaw area fraction determined was equivalent to the volume fraction, relative density of each sample was determined.

X-Ray diffraction (XRD) was performed using PANalytical Empyrean™ diffraction system with 1.8 kW Cu X-ray tube operating at 45 keV voltage and 40 mA current. A Cu-k_α radiation source with wavelength of 1.54 Å was utilized. For each alloy sample, XRD was performed with a step size of 0.02º within 2θ range of 20°–100°, with a dwell time resulting in a minimum of 10,000 counts at the highest intensity peak. To observe the melt-pool and grain structure, as-built specimens were etched using Keller's reagent for optical microscopy. Further microstructural examination was conducted using Zeiss™ Ultra-55 field emission scanning electron microscope (FE-SEM) equipped with X-ray energy dispersive spectroscopy (XEDS). Microstructural features on selected samples were examined by using transmission electron microscope (FEI/Tecnai™ F30 TEM) operating at an accelerating voltage of 300 kV, equipped with XEDS detector and Fischione™ high angle annular dark field (HAADF) detector. Site-specific TEM samples were prepared using FEI™ TEM 200 focused ion beam (FIB) via in-situ lift-out (INLO) method. Grain orientation mapping was performed using electron back scatter diffraction (EBSD, EDAX), with a resolution of 0.8 µm for mapping unmodified AA6061, and 0.4 µm for mapping the Zr-modified AA6061.

3. Results and analyses

3.1. Characteristics of gas atomized powders

Table 1 reports the composition of unmodified and Zr-modified AA6061 powders measured via XEDS, and Fig. 2 presents characteristics of gas atomized powders for both compositions. The morphology of gas-atomized powders, presented in Fig. 2(a) and (d), demonstrated that most of the powders exhibited near spherical geometry. Fig. 2(a, b) and (d, e) show the microstructure of the unmodified and Zr-modified AA6061 gas-atomized powders, respectively. Both consisted of primary α-Al dendrites with solute-enriched interdendritic regions. Fig. 2(c) and (f) present the powder size distribution of the unmodified and Zr-modified AA6061 gas-

atomized powders, respectively. The average powder diameter (D), along with D_{10}, D_{50} and D_{90} values for the unmodified and Zr-modified AA6061 gas-atomized powders are reported in Table 2.

Table 1. Composition (wt%) determined by XEDS for the commercial, unmodified AA6061 and Zr-modified AA6061 alloy powders produced by gas atomization.

AA6061	Al	Mg	Si	Ti	Cr	Mn	Fe	Ni	Cu	Zn	Zr
Commercial	Bal.	1.14	0.78	0.11	0.24	0.09	0.28	0.10	0.21	0.06	–
Modified	Bal.	0.96	0.69	0.10	0.18	0.08	0.19	0.04	0.18	0.03	0.99

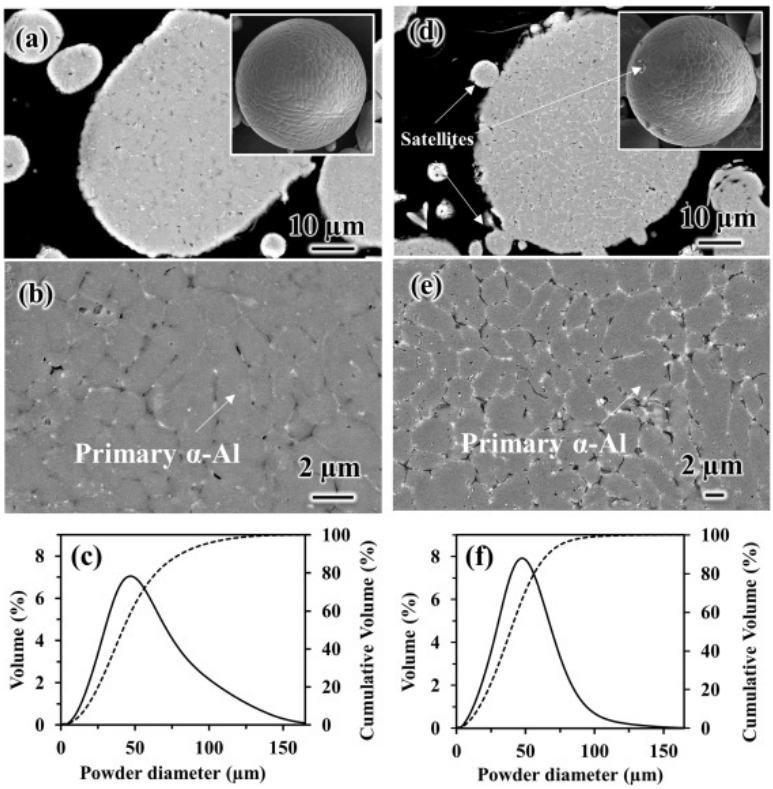

Fig. 2. Characteristics of (a–c) unmodified and (d–f) Zr-modified AA6061 alloy powders:
(a,d) backscatter electron cross-sectional micrograph with inset of secondary electron micrograph; (b,e) high magnification backscatter electron cross-sectional micrograph; and (c,f) powder size distribution of gas-atomized powders.

Table 2. Powder size distribution of unmodified and Zr-modified AA6061 alloy powders.

AA6061	Average, D (µm)	D_{10} (µm)	D_{50} (µm)	D_{90} (µm)
Unmodified	50.58	19.44	45.72	88.98
Zr-Modified	44.27	16.92	42.59	72.81

Fig. 3 presents XRD patterns from unmodified and Zr-modified AA6061 powders. Both powders mainly exhibited the presence of α-Al (FCC). Despite the low intensity, XRD from $Al_{19}Fe_4MnSi_2$ phase was observed, and Zr-modified AA6061 also showed the presence of Al_3Zr phase. No Mg_2Si peaks were observed in either powder.

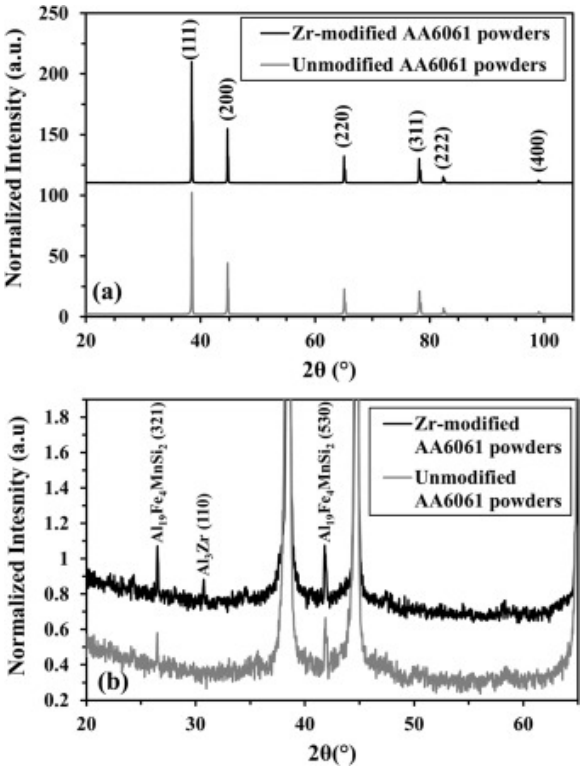

Fig. 3. X-ray diffraction patterns from unmodified and Zr-modified AA6061 powders: (a) overall patterns from 20° to 100° in 2θ; and (b) detailed patterns from 20° to 60° in 2θ.

3.2. LPBF parameters and flaw characterization

Fig. 4 presents relative density of the as-built, (a) unmodified and (b) Zr-modified AA6061 fabricated using LPBF with varying laser power and scan speed. Theoretical density of unmodified and Zr-modified AA6061 employed was 2.70 and 2.71 g/cm^3, respectively. For the as-built, unmodified AA6061 alloy fabricated at 200 W, the relative density increased initially with an increase in scan speed from 100 mm/s, and had a maximum value of 97.6% at 300 mm/s, but decreased further with higher scan speed up to 800 mm/s. A similar trend was observed at 350 W, but starting with a very low value of relative density as presented in Fig. 4(a). The relative density sharply increased from 400 mm/s to 1000 mm/s, had a maxima at 97.5%, and then decreased and remains constant from 1000 to 1800 mm/s.

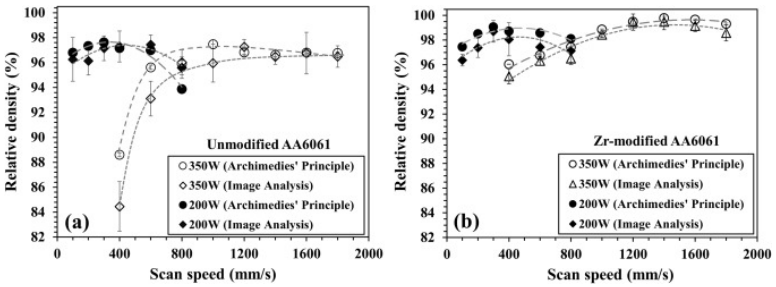

Fig. 4. Relative density of the as-built, (a) unmodified and (b) Zr-modified AA6061 fabricated using LPBF with varying laser power and scan speed.

For the Zr-modified AA6061 alloy fabricated at 200 W, the relative density first increased and then decreased as the scan speed varied from 100 to 800 mm/s, with the maximum density of 97.6% at 300 mm/s as presented in Fig. 4(b). Similarly at 350 W, density first increased as the scan speed increased from 400 mm/s to 1400 mm/s,

had a peak value of 99.7%, and slightly decreased as the scan speed further increased to 1800 mm/s. Fig. 4 also presents the relative density determined by quantitative image analysis using the optical micrographs. Changes in relative density as a function of scan speed were similar to those determined by Archimedes' method, but the magnitude of relative density was, in general, lower for the values determined by image analysis.

Fig. 5(a) shows the XY and XZ cross-sectional optical micrographs from the as-built unmodified AA6061 as a function of scan speed at a laser of 200 W. Extensive cracks and porosity were observed in all samples. At lower scan speeds, porosity was mainly spherical due to higher energy density (i.e., keyhole porosity). The amount of spherical porosity decreased with an increase in scan speed, but at higher scan speeds, non-spherical/irregular flaws appeared due to lack of fusion (i.e., insufficient energy input). Regardless, significant cracking was observed at all scan speeds for unmodified AA6061 fabricated by LPBF at 200 W. In XY cross-sections, cracks appeared as cellular network, and the extent of the cracks decreased with an increase in scan speed. Cracks were oriented in the build-direction, Z, in the XZ cross-sections as shown in Fig. 5(a).

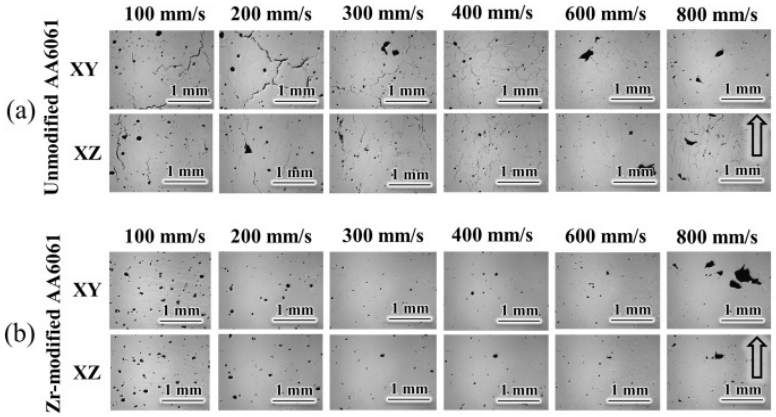

Fig. 5. Optical micrographs from the XY and XZ cross-sections of the as-built (a) unmodified AA6061 and (b) Zr-modified AA6061 at a laser power of 200 W with varying scan speed. Arrows indicate the build direction.

Fig. 6(a) shows the XY and XZ cross-sectional optical micrographs from the as-built, unmodified AA6061 as a function of scan speed at a laser of 350 W. Similar to Fig. 5(a), all samples had extensive presence of cracks and porosities. The amount of porosity decreased with an increase in scan speed up to 1200 mm/s, but increased thereafter possibly due to transition from keyhole porosity to lack of fusion flaws [35]. Cellular network and vertically oriented cracks on the XY and XZ cross-sections, respectively, were present regardless of scan speed. However, cracking increased with higher scan speeds as presented in Fig. 6(a).

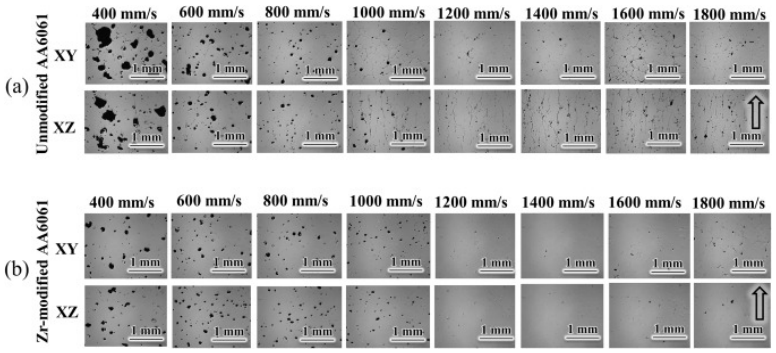

Fig. 6. Optical micrographs from the XY and XZ cross-sections of the as-built (a) unmodified AA6061 and (b) Zr-modified AA6061 at a laser power of 350 W with varying scan speed. Arrows indicate the build direction.

Figs. 5(b) and 6(b) presents the optical micrographs from the as-built, Zr-modified AA6061 fabricated using laser power of 200 W and 350 W, respectively. Overall, compared to the unmodified AA6061 samples shown in Figs. 5(a) and 6(a), a slight decrease in the amount of porosity and lack-of-fusion flaw was observed. Still, spherical porosity at low scan speed, and irregularly-shaped, lack-of-fusion flaws were present as a function of scan speed. But there is a remarkable disappearance of cracking for all LPBF parameters examined, except for minor crack-like features found at 1600 and 176 1800 mm/s scan speed and laser power of 350 W.

The crack density in both unmodified and Zr-modified AA6061 was measured using the quantitative image analysis as presented in Fig. 7. Crack density was defined as the overall length of the crack per unit area from at least 5 optical micrographs from each sample, either in XY and XZ cross-section. Fig. 7(a) shows that the crack density in unmodified AA6061 is in general higher in XY cross-section than in XZ cross-section, and is significantly higher than the crack densities found in Zr-modified AA6061 at 200 W. Fig. 7(b) shows that the crack density in unmodified AA6061 monotonically increased with an increase in scan speed at 350 W. More importantly, similar to samples produced at 200 W, Zr-modified AA6061 exhibited a significant reduction in crack density. Therefore, the addition of Zr resulted in a significant improvement in LPBF printability/buildability of AA6061. The sample fabricated at the scan speed of 1400 mm/s had the highest relative density of 99.7%, and was examined in detail for microstructure and mechanical properties.

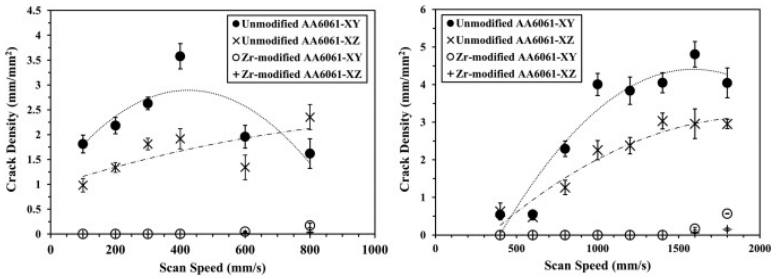

Fig. 7. Solidification crack density in the as-built, unmodified and Zr-modified AA6061 alloys determined from the XY and YZ cross-sections using ImageJ as a function of scan speed using laser power of (a) 200 W and (b) 350 W.

3.3. Composition, microstructure and crystallographic texture

Concentration of the constituent elements in as-built, unmodified and Zr-modified AA6061 alloys fabricated at 350 W was measured using XEDS. Concentrations of the main alloying additions such as Fe, Mn, Si, Cu and Zr have remained relatively constant as a function of scan speed, however that of Mg varied as a function of scan speed. Fig. 8 shows the variation in the concentration of the Mg, Si and Zr. These would influence the formation of the strengthening precipitates (i.e. Mg_2Si in unmodified AA6061, and Mg_2Si and Al_3Zr in Zr-modified AA6061). Concentrations of Si and Zr remained relatively constant as a function of scan speed, but that of Mg decreased as the scan speed decreased, both in unmodified and Zr-modified AA6061. The loss of Mg during LPBF process with lower scan speed (i.e., high energy density) can be attributed to the higher vapor pressure of Mg [36], [37]. Higher energy density associated with slower scan speed results in higher melt-pool temperature [38] and slow cooling rate (i.e. longer solidification time) [39]. Prolonged, high temperature would promote the vaporization of Mg [40].

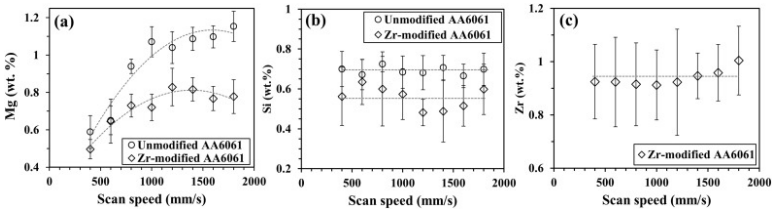

Fig. 8. Variation in concentration of (a) Mg, (b) Si, and (c) Zr in unmodified and Zr-modified AA6061 alloys as a function of scan speed at 350 W power.

Fig. 9 presents backscatter electron (BSE) micrographs from the XZ cross-sections of the as-built alloy specimens fabricated at 350 W power and 1400 mm/s scan speed. From the unmodified AA6061, multiple cracks were observed, oriented in the build direction as presented in Fig. 9(a), and large columnar grains, indicated by the dotted lines in Fig. 9(b), which were mostly parallel to the orientation of the cracks. Both cracks and columnar grains were much larger than the typical height of the melt-pool in the build direction. The high magnification micrograph in Fig. 9(c) depicts the region containing melt-pool boundaries which is devoid of any distinguishable features (e.g., dark spots are the etch pits). Fig. 9(d)–(f) present the BSE micrographs from the as-built, crack-free Zr-modified AA6061 with equiaxed grains near melt pool boundaries as shown in Fig. 9(e) and fine columnar grains within melt pools as shown in Fig. 9(f). The fine columnar grains within melt pools were typically normal to the melt pool boundaries.

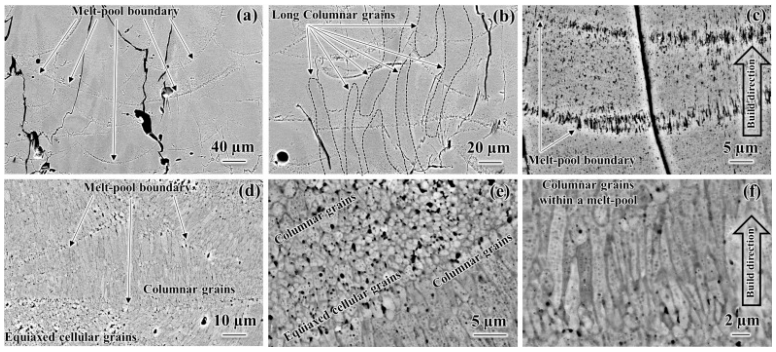

Fig. 9. Backscatter electron micrographs from the XZ cross-sections of the as-built (a–c) unmodified AA6061 and (d–f) Zr-modified AA6061 alloys.

Fig. 10 presents X-ray diffraction patterns from the unmodified and Zr-modified AA6061 alloys in both the XY and XZ orientations. Strong crystallographic texture was observed in both the XY and XZ cross-sections in as-built, unmodified AA6061 for (200) peak, as seen in Fig. 10(a), corresponding to the preferential orientation of grains along the <100> direction. This texture was further corroborated by the EBSD grain orientation maps wherein large columnar grain can be observed in the build direction, which yielded a symmetric pole figure with a strong intensity at the center of the (001) pole figure from the XY cross-section and a strong intensity at the north and south poles of (001) pole figure from teh XZ cross section, as shown in Fig. 11(a) and (b), respectively. In LPBF, repeated melting/heating and solidification/cooling would produce thermal gradient primarily along the build direction (i.e. <100> direction). For cubic metal, grain growth is preferred along the <100> due to its least packing efficiency. Therefore, most grains grew in the build orientation along <100> crystallographic direction, consistent with the previous investigations of the LPBF of unmodified AA6061 [24], [27], [29] and other commercial Al-alloys, e.g. AA5083 [20]. A substantial reduction in preferential texture was observed in the as-built, Zr-modified AA6061 as presented by the XRD in Fig. 10(a). Pole figure maps from the as-built Zr-modified AA6061 exhibited similar behavior as in unmodified alloys, however with a significantly weaker degree of crystallographic texture. This significant reduction in crystallographic texture would be attributed to the

significant grain refinement effect due to development of equiaxed grains along the melt pool boundaries and fine columnar grains confined within melt-pools, as shown in Figs. 9(e), 9(f), 11(c) and 11(d). Fig. 11(e) shows that the grain size in the as-built, unmodified AA6061, ranged from 5 to 80 µm and from 8 to 130 µm in the XY and XZ orientations, respectively. However, with the addition of 1 wt% Zr in AA6061, grain sizes were reduced to 0.6–10 µm and 0.7–21 µm in the XY and YZ orientations, respectively.

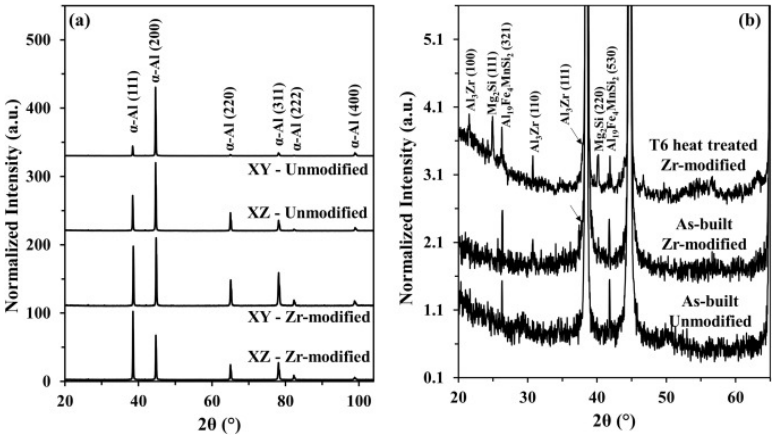

Fig. 10. (a) XRD patterns from the as-built, unmodified and Zr-modified AA6061 alloys; (b) Details of XRD patterns from the XZ cross-sections of unmodified and Zr-modified AA6061 that demonstrate the development of relevant precipitates, Mg_2Si and Al_3Zr.

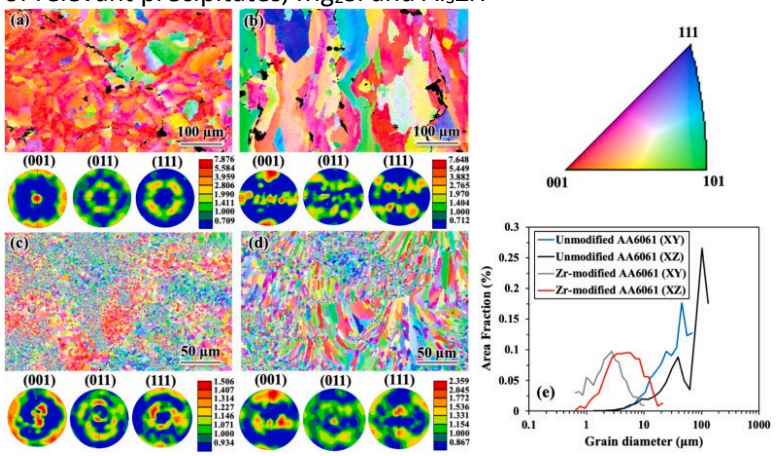

Fig. 11. Inverse pole figure grain orientation mapping of as-built, unmodified AA6061 from the (a) XY and (b) XZ cross-sections; those of as-built, Zr-modified AA6061 from the (c) XY and (d) XZ cross-sections; (e) grain size distribution in unmodified and Zr-modified AA6061 fabricated by LPBF.

Details of X-ray diffraction patterns from unmodified and Zr-modified AA6061 are presented in Fig. 10(b). In all patterns, α-Al matrix and $Al_{19}Fe_4MnSi_2$ dispersoid phase were present. Our previous work [3] of AA6061 had comprehensively documented the microstructural characterization of the precipitates (i.e., $Al_{19}Fe_4MnSi_2$, Mg_2Si, in AA6061 alloy using electron diffraction studies via TEM). The presence of Al_3Zr in the as-built, Zr-modified AA6061 was confirmed by XRD pattern. TEM investigation from the fine grain region (near the melt-pool boundary) suggest that the grain boundaries is decorated with the low melting intermetallic $Al_{19}Fe_4MnSi_2$ compounds, as shown in Fig. 12(a). Furthermore, Al_3Zr precipitates in as-built Zr-modified AA6061 exhibits cuboidal morphology, as shown in Fig. 12(b), which is similar to the cuboidal shape of Al_3Zr observed during LPBF of Zr-modified AA5083 [20]. The Mg_2Si precipitates were not observed in both the as-built, unmodified and Zr-modified AA6061, presumably due thermo-kinetic environment associated with LPBF (i.e., supersaturated Mg and Si [41]).

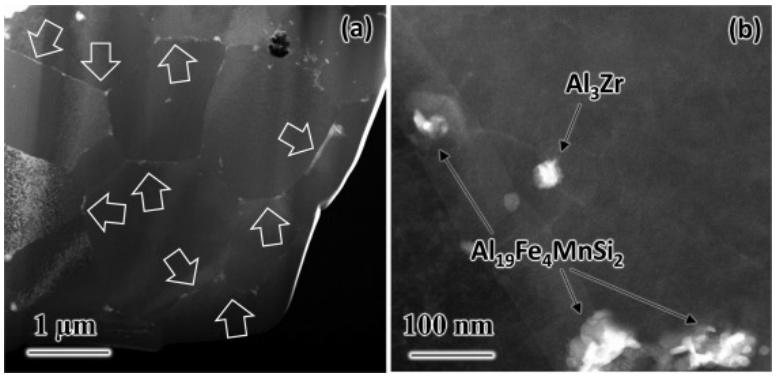

Fig. 12. High angle annular dark field (HAADF) micrographs from the fine grain region (along melt-pool boundary) of the Zr-modified AA6061 depicting the presence of (a) $Al_{19}Fe_4MnSi_2$ precipitates decorated at the grain boundaries as indicated by arrows; and (b) cuboidal Al_3Zr precipitates along with some irregular $Al_{19}Fe_4MnSi_2$ precipitates in grain interior.

The as-built, Zr-modified AA6061 was subjected to the standard, two-step T6 heat treatment for precipitate strengthening. LPBF samples were first solutionized at 500 °C for 1 h and then artificially aged at 160 °C for 10 h. Solution heat treatment at 500 °C would help in precipitating the additional Al_3Zr phase, while solutionizing the other alloying additions. Although the ideal temperature to precipitate Al_3Zr ($L1_2$) from α-Al matrix is approximately 400 °C for 2 h [42], this would result in simultaneous precipitation and excessive growth of the Mg_2Si precipitates based on pseudo-binary phase diagram between Mg_2Si and α-Al [41]. The subsequent artificial aging heat treatment at 160 °C would not result in any significant growth of Al_3Zr due to its small diffusivity ($\widetilde{D}_{Al/Zr}^{int,Al_3Zr} \approx 6.1 \times 10^{-21}$ m^2/s at) at 160 °C [7] which corresponds to diffusion distance of about 15 nm $\left(\sqrt{\widetilde{D}_{Al}^{int} t}\right)$ in 10 h. The XRD pattern from the T6 heat-treated, Zr-modified AA6061 is presented in Fig. 10(b). The emergence of Mg_2Si precipitates and an increase in relative intensity of Al_3Zr (100) are clear. The presence of Al_3Zr (100) peak suggested that the T6 heat treated Al_3Zr had $L1_2$ crystal symmetry, which would contribute towards strengthening.

3.4. Mechanical properties

Table 3 reports the hardness determined from Vickers and instrumented-indentation for the as-built and heat treated Zr-modified AA6061. Hardness values were approximately similar for the samples that were as-built and solution heat treated (SHT). Presence of residual stress associated with LPBF would contribute significantly to the hardness for the as-built sample [43]. So, the hardness should decrease after SHT due to stress-relieving effect and homogenization. However, for the LPBF Zr-modified AA6061, hardness remained similar presumably due to additional precipitation of Al_3Zr during solutionizing at 500 °C. Subsequent artificial aging at 160 °C for 10 h resulted in the precipitation of Mg_2Si, which increased the hardness of Zr-modified AA6061 as reported in Table 3. Fig. 13(a) shows the load-displacement curves from the different heat treated conditions of the Zr-modified AA6061. The penetration depth is maximum for the SHT samples which corresponds to the minimum hardness and minimum for the T6 heat treated samples which corresponds to the maximum hardness, which is in accordance with hardness data, provided in Table 3.

Table 3. Comparison of Vickers (VHN) and instrumented-indentation hardness (H) of LPBF fabricated Zr-modified AA6061 in the as-built condition, after solution heat treatment, and after artificial aging according to the standard, two-step T6 heat treatment.

Heat treatment condition	**Vickers**	**Nano-indentation**		

	VHN (Hv)	H (GPa)	E_r (GPa)	E (GPa)
as-built	88.6 (0.4)	1.34 (0.1)	77.0 (3.0)	73.5 (3.0)
After SHT at 500 °C for 1 h	87.4 (0.6)	1.28 (0.1)	77.3 (2.4)	73.9 (2.4)
After aging at 160 °C for 10 h	111.7 (0.7)	1.65 (0.1)	77.0 (3.1)	73.5 (3.2)

Fig. 13(b) presents the engineering tensile stress-strain curves for the as-built and T6 heat treated Zr-modified AA6061 alloy produced with laser power of 350 W and scan speed of 1400 mm/s. Both the as-built and T6 heat treated tensile specimens initially deformed elastically, and then strain hardened until fracture. The as-built, Zr-modified AA6061 had yield strength (YS, $\sigma_{0.2}$) of 209–212 MPa and ultimate tensile strength (UTS) of 267–269 MPa with an elongation at fracture (El%) of 25.3–27.6%. After T6 heat treatment, YS increased to 290–308 MPa and UTS improved to 318–335 MPa with the reduction in El% to 13.2–14.2%. Numerical results from the tensile testing are reported in Table 4.

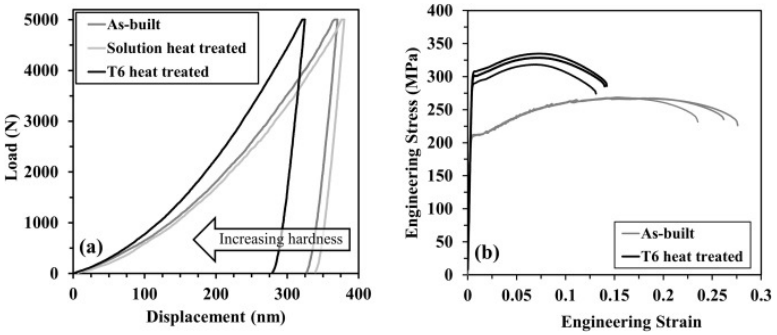

Fig. 13. (a) Load-displacement curves and (b) engineering stress-strain curves of LPBF Zr-modified AA6061 alloy in the as-built and heat-treated conditions.

Table 4. Room temperature tensile properties for LPBF Zr-modified AA6061 in the as-built condition and after T6 heat-treatment along with comparison to other reported values for AA6061. Standard deviation in property is in parenthesis.

Heat treatment	YS (MPa)	UTS (MPa)	El (%)	E (GPa)	Reference
As-built Zr-modified AA6061	210.3 (1.1)	268.1 (0.5)	26.5 (0.9)	70.1 (0.3)	This study
T6 heat-treated Zr-modified AA6061	299.8 (7.2)	327.3 (6.8)	13.9 (0.4)	70.0 (0.3)	This study
As-cast AA6061	60–120	150–250	12–15	68.9	[44]
O-annealed wrought AA6061	55	125	25	68.9	[44]
T6 heat-treated wrought AA6061	276	310	12	68.9	[44]
As-built AA6061 printed on 200 °C heated build plate	246.7	392	3.9	–	[30]
As-built AA6061 printed on 500 °C heated build plate	60	140	15	–	[29]
T6 heat treated printed on 500 °C heated build plate	280	310	3.5	–	[29]
As-built Sc-modified AA6061	300	350	31	–	[28]
YSZ-modified AA6061	*Mechanical properties were not investigated*				[27]
ZrH_2 modified AA6061					[26]

Table 4 also compares reported tensile properties of traditionally fabricated wrought AA6061 after various heat treatments [44] and additively manufactured AA6061 [26], [27], [28], [29], [30]. In the annealed condition (O), AA6061 exhibits the highest elongation up to 25%, and this is comparable with the elongation in the as-built condition of Zr-modified AA6061 (up to 27.6%). However, the as-built Zr-modified AA6061 has significantly higher YS (> 3X) and UTS (> 2X) than the AA6061 in O-annealed condition. After T6 heat treatment, LPBF Zr-modified AA6061 exhibited higher YS and UTS than the T6-treated wrought AA6061. The as-built AA6061 fabricated on the pre-heated build plate at 200 °C yielded high YS of 247 MPa and UTS of 392 MPa, but a substantially low fracture strain ~3.9% [30]. When the build plate was preheated to 500 °C, YS and UTS were reduced to 60 MPa and 140 MPa, respectively, with a fracture strain ~15% [29]. Subsequent T6 heat treatment of LPBF AA6061 that was printed on a 500 °C heated build plate improved the YS and UTS to 280 MPa and 310 MPa, respectively, but further reduced the fracture strain down to 3.5% [29]. Interestingly, the as-built Sc-modified AA6061 exhibited excellent YS and UTS of 300 MPa and 350 MPa, respectively, in addition to a high fracture strain of 31%.

Fig. 14 shows the fractured surfaces from the as-built and T6 heat-treated Zr-modified AA6061 alloy. In the as-built alloy, fractured surface consisted of large dimples and cleavage facets, while in T6 heat treated alloy, much smaller dimples were present. These features are indicative of ductile fracture, and the larger dimples found in as-built samples may be related to higher ductility [45].

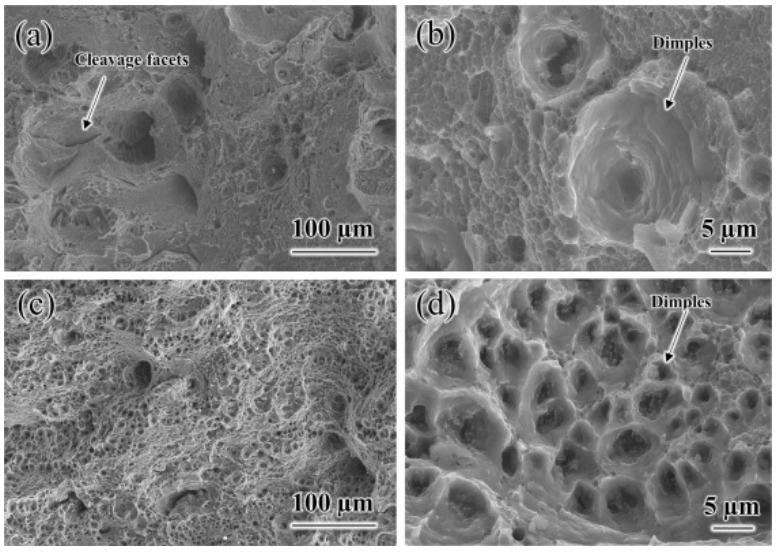

Fig. 14. Secondary electron micrographs of the fracture surfaces from the (a, b) as-built and (c, d) T6 heat treated Zr-modified AA6061 alloy.

4. Discussion

4.1. Cracking in AA6061

Unmodified AA6061 with Si and Mg as major alloying additions falls under the category of the Al-Si-Mg based alloys. Present investigation demonstrated that the unmodified AA6061 composition suffers from the poor printability/buildability. The AlSi10Mg alloy, which is also Al-Si-Mg based alloys, exhibits excellent LPBF printability/buildability [13]. Compositionally, AA6061 and AlSi10Mg have a similar Mg content of 0.8–1.2 and 0.2–0.45 wt%, respectively, but substantially different Si content, e.g., 0.4–0.8 wt% Si in AA6061 versus 9–11 wt% Si in AlSi10Mg. Excellent printability of AlSi10Mg is often attributed to the melt flowability/fluidity, low shrinkage and narrow solidification range associated with near eutectic composition [13]. Therefore, Al-Si based alloys with near-eutectic compositions are in general

compliant with power bed fusion based AM technologies [21]. Hyer et al. [17], [46] conducted a systematic investigation on the printability of the Al-Si alloys as a function of Si content, and observed that alloys with ~0.5–1.0 wt% Si exhibited the maximum solidification cracking susceptibility tendency. Solidification cracking tendency was maximum for other alloys with compositions of: 0.3–0.4% Fe, 0.5% Mg, 0.5% Si and 0.15% Ti [47], which also aligns well with the composition of the unmodified AA6061. In fact, AA6061 exhibits maximum solidification cracking susceptibility among many commercial Al-alloys e.g. AA7075, AA 2219, AA2024 etc. [10].

Solidification cracking is frequently associated with the shrinkage from liquid-to-solid transformation, which is reported to be 6.6% for Al [48]. Near the terminal stage of the solidification, solute enriched melt would be highly unstable and undercooled, which would produce local interdendritic channels with a thin layer of trapped liquid [49] and the mushy zone. During LPBF of unmodified AA6061, the grain boundaries would be decorated with low melting Al, Fe, Mn, Si rich intermetallic compounds due to solute segregation (e.g., Fig. 12(a)), and result in thin continuous semi-solid liquid film, due to thermal gradient, between adjacent, long columnar grains. Furthermore, due to the highly localized nature of melting and faster cooling rates associated with LPBF, the associated shrinkage can be classified as *obstructed shrinkage*, which would induce tensile stresses in the mushy zone.

The microstructure of LPBF-fabricated, unmodified AA6061 exhibited long columnar grains, as shown in Fig. 9(a) and (b) along the build direction, which also corresponds to <100> and the direction of thermal gradient. These large columnar grains spanned over a minimum of two to three melt-pool layers, which demonstrate the epitaxial growth of grains with successive melting [20]. These large columnar grains would be inadequate to accommodate the tensile strains generated during obstructed shrinkage [50]. Moreover since the mushy zone has limited ductility [10], these tensile stresses would shear/tear the mushy melt apart during the terminal stages of solidification, resulting in cracks. Sonawane et al. [24] suggested that the cracks in AA6061 preferentially develop near the center of the melt-pool at high-angle grain boundaries (HAGBs) with misorientation angle greater than 15°, while low-angle grain boundaries and/or HAGBs away from the center of the melt pool remain un-cracked. Nucleation of the crack at the central region of the melt-pool at the high angle boundaries can occur due to the high pressure drop of the solidifying liquid flowing in the HAGBs. More details on the cracking mechanism of commercial AA6061 and the influence of LPBF processing parameters on cracking susceptibility in AA6061 have been reported by Sonawane *et* al. [24]. Furthermore, Fig. 9(a), 9(b), and 11(b) also show the solidification cracks with substantial thickness, spread over multiple melt-pool layers. This observation suggests that the initially nucleated cracks grew epitaxially with successive melting along the long columnar grain-boundary.

Kou and co-workers [10], [51], [52], [53] suggested that smaller dihedral angles associated with long columnar grains has a deep crack channel, as illustrated in Fig. 15, which needs to be filled with liquid during subsequent melting to avoid crack growth. Thus, directional or epitaxial tendency of the solidification crack growth is largely motivated by the inability of molten AA6061 to refill the pre-existing crack from the previous layer, owing to its poor melt fluidity and faster cooling rates associated with LPBF [52]. If the cracks are not healed by the liquid, then it can act as the seed for further crack growth during LPBF. Epitaxially grown cracks would often be deflected by the new melt-pool layer, and generally grow normal to the tangent of the melt-pool boundary as shown in the Fig. 9(a). This process would continue with the subsequent addition of new layer, and the growth front of the crack would eventually close after multiple deflections at the melt-pool boundary. There were also many small narrow cracks, oriented along the build direction, confined within a melt-pool. In this case, the molten AA6061 from the subsequent melting of the next powder layer was able to cover the top end of the crack and solidify before it refilled the pre-existing cracks.

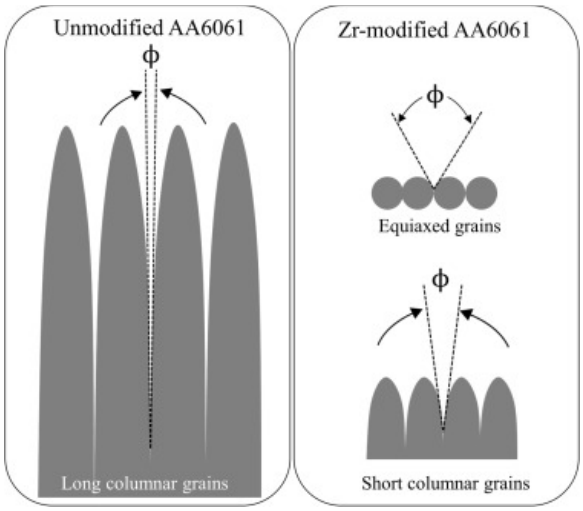

Fig. 15. Schematic representations of dihedral angle (ϕ) of grains in (a) unmodified and (b) Zr-modified AA6061.

Kou and co-workers [10], [51], [52], [53] also developed the criteria for predicting the crack susceptibility using the alloy solidification curve (T vs. $f_s^{1/2}$) based on the Gulliver and Scheil model [54]. In this model, steepness of the solidification curve at the terminal stages of the solidification ($f_s \rightarrow 1$) is directly related to the crack susceptibility of an alloy. Fig. 16 presents the solidification curves for the unmodified and Zr-modified AA6061, and shows that the addition of Zr does not change the solidification curve [26], [55] as $f_s \rightarrow 1$. Thus the unmodified AA6061 and Zr-modified AA6061 have similar crack susceptibility [51]. However, Figs. 7, 9, and 11 shows that cracking in Zr-modified AA6061 is completely eliminated, which would be due to changes in its *liquid metal property* and *grain refinement effect*. Zr in Al-alloys is known to reduce the solid/liquid interfacial energy and decrease the surface tension of liquid melt owing to its surface active properties [56]. Surface tension (γ) of the melt-pool can be related to the dynamic viscosity (μ) of the liquid melt by [57]: $\mu = 16/15\sqrt{m/kT}\,\gamma$, where m is the atomic mass, T is the melt temperature, and k is the Boltzmann constant. Therefore, addition of Zr (i.e., surface active element) also correspond to the reduction in the viscosity of the liquid melt, which would allow the flow of the melt through the crack channel. Furthermore, lowering in surface tension can also reduce the thermal gradient in the liquid melt [55].

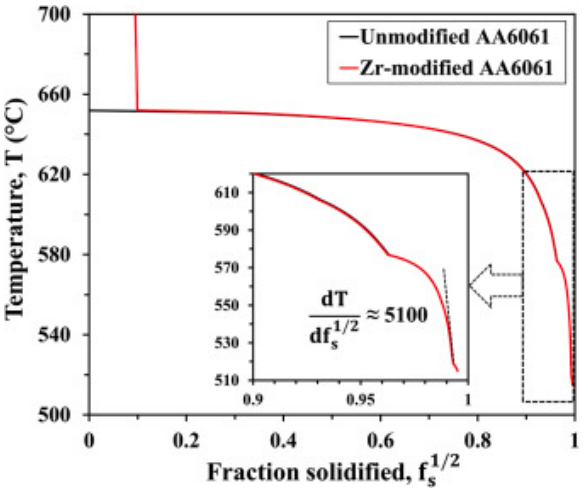

Fig. 16. Solidification curves of unmodified and Zr-modified AA6061, constructed with the help of Thermo-CalcTM software using TCAL7 thermodynamic database.

The Zr concentration in the Zr-modified AA6061 was approximately 1 wt%. This is higher than the solubility limit of Zr in Al based on the binary Al-Zr phase diagram [58]. Therefore, Zr-modified AA6061 alloy, examined in this work, is deliberately designed to form pro-peritectic Al_3Zr during solidification. Figs. 9(e), 9(f), and 11 demonstrate the significant grain size reduction in as-built, Zr-modified AA6061 along with the formation of Al_3Zr. The Al_3Zr has the highest melting temperature among all the precipitates observed in Zr-modified AA6061, and the amount of Zr added was intended to change the primary phase to solidify Al_3Zr first, and not the α-Al (fcc) and/or $Al_{19}Fe_4MnSi_2$ phase. Glerum et al. [59] had demonstrated via high-speed in situ synchrotron X-ray imaging and diffraction during the LPBF of Al-1.5Zr alloy, that the Al_3Zr phase forms in the Al-rich molten melt-pool with $L1_2$ crystal symmetry. The $L1_2$ Al_3Zr would impart low energy of nucleation barrier for the heterogeneous nucleation of α-Al grains in a liquid melt-pool because of similarity in crystal structure and lattice parameter of $L1_2$ Al_3Zr and α-Al. The primary Al_3Zr particles would typically form at the bottom of the melt-pool (i.e., boundary) where the solidification front velocity is slow [20], and act as a nucleation site for the formation of fine grains. Therefore, fine equiaxed grains were observed along the melt-pool boundary. Relatively faster solidification front velocity in the middle and the near-the-top of the melt-pool would result in supersaturation of Zr in α-Al [60]. This yields shorter columnar grains orthogonal to the melt-pool boundary. The columnar grains in Zr-modified AA6061 were significantly shorter/smaller than in unmodified AA6061 and were all confined within a melt-pool, because with the melting of subsequent powder layer, band of small equiaxed fine grains would form at the bottom of the next melt-pool along the melt pool boundary, which would disrupt the epitaxial development of large, columnar grains.

The shorter columnar grains in Zr-modified AA6061 correspond to relatively larger dihedral angles and shallow liquid channel between two adjacent grains. Fine equiaxed grains have the largest dihedral angle, as schematically presented in Fig. 15. For the Zr-modified AA6061, it would be easier to refill the shorter crack channels between adjacent grains [52] with the less-viscous molten liquid. Furthermore, fine equiaxed grains can accommodate tensile strain more efficiently than the long columnar grains [50], and thus resistant to solidification cracking. For the samples fabricated with optimized LPBF parameters, columnar grains growing on top of the band of small equiaxed grains (confined within a melt-pool) may exhibit misorientation lower than 15°, and thus without cracking [24].

In addition, even if any pre-existing cracks have not been healed by the molten metal, formation of fine grains at the melt-pool boundaries would suppress any propagation of the solidification cracking beyond individual melt-pools. Fig. 5, Fig. 6, Fig. 7 show that cracks were eliminated, except for minor cracking observed when higher laser scan speed (≥ 1600 mm/s) was used at a laser power of 350 W. This may be due to a faster cooling rate associated with a higher scan speed, which could yield more supersaturation of Zr in α-Al matrix (i.e., lower amount of Zr available to form Al_3Zr inoculation). Moreover, faster cooling would result in solidification of liquid melt before refilling the pre-existing cracks. Additional details for the mechanism of grains refinement and crack suppression in Zr-modified Al-alloys can be found in the work of Zhou et al. [20].

4.2. Porosities and flaws in AA6061

Figs. 5(a) and 6(a) show that the porosity and/or flaws in unmodified AA6061 is related to the scan speed. The amount of porosity and/or flaws generally decreased with an increase in scan speed to achieve a minima at intermediate scan speeds, but increased thereafter with a further increase in scan speed. In this work, scan speed was varied at a constant laser power, therefore, percentage flaws can be related to the energy density, which is inversely related to the scan speed, and examined with respect to the melting mode (i.e. keyhole or conduction mode on the basis of study by Qi et al. [35]). At 350 W laser power and 400 mm/s scan speed, a significant amount of porosity was observed due to the very high energy density (224.3 J/mm^3), which would generate the highest melt temperature and the deepest laser penetration. This would result in the trapping of pores at the bottom of the deep melt-pool after solidification (i.e., keyhole mode). As the energy density

decreased from 224.3 J/mm^3 (at 400 mm/s), fraction porosity decreased to a minimum at an energy density of 64.1 J/mm^3 (at 1400 mm/s). With a further decrease in energy density, lack-of-fusion flaws increased due to insufficient laser energy, which may possibly correspond to the either conduction mode or transition between keyhole to conduction mode. A similar trend was observed for the Zr-modified AA6061. Specimen fabricated with an energy density of 64.1 J/mm^3 (at 1400 mm/s) exhibited the least porosity. The overall amount of porosity and/or flaws in Zr-modified AA6061 was, however, lower than that in unmodified AA6061. Zhou et al. [20] suggested that this may be attributed to the change in properties such as melting point, melt viscosity, thermal conductivity and laser absorptivity.

4.3. Mechanical properties

Yield strength of Zr-modified AA6061 alloy was higher than traditionally manufactured wrought AA6061 alloy after T6 heat treatment with similar ductility as shown in Table 4. AA6061 is a precipitation hardenable alloy strengthened by the formation of Mg_2Si precipitates after T6 heat treatment. In Zr-modified AA6061, both the Al_3Zr and Mg_2Si would contribute to the strengthening. Ideally, heat treatment at 400 °C for 2 h is recommended to strengthen the α-Al matrix with metastable $L1_2$ Al_3Zr precipitates [20], [42], however this would simultaneously precipitate and coarsen the Mg_2Si in AA6061. Therefore, SHT was initially conducted at 500 °C for 1 h to solutionize Mg_2Si and simultaneously artificially age the metastable Al_3Zr.

Precipitation strengthening are governed by either the Orowan dislocation bypassing mechanism or dislocation shearing mechanism [61]. In the Orowan mechanism, increase in yield strength occurs when the moving dislocation is required to loop around the obstructing coherent precipitate. This increase in yield strength is expressed by [61], [62]:

(2)

$$\Delta\sigma_{orowan} = M\frac{0.4Gb}{\pi\sqrt{1-\nu}}\frac{\ln(2\bar{r}/b)}{\lambda_p}$$

where M is the Taylor mean orientation factor for the FCC Al (3.06), G is the shear modulus of Al (25.4 GPa), b is the burger's vector ($a_o\sqrt{2}$) in Al (2.86 Å), ν is the poisson's ratio of Al (0.334) and $\bar{r}$ is the average size precipitate cross section in random plane, $\bar{r} = \sqrt{2/3}\,r$, and r is the radius of the precipitate. The λ_p represents the inter-precipitate spacing, which can be estimated from: $\lambda_p = 2\bar{r}(\sqrt{\pi/4f} - 1)$, where f is the volume fraction of the precipitates.

In dislocation shearing mechanisms, an increase in yield strength is contributed by three factors: coherency strengthening (σ_{cs}), modulus mismatch strengthening (σ_{ms}) and ordering strengthening (σ_{os}). Coherency strengthening and modulus mismatch strengthening mechanisms operates before the dislocation shears the precipitates, while ordering strengthening operates during shearing the precipitates. Coherency strengthening (σ_{cs}) is associated with the difficulty in dislocation motion due to strain-field interaction, and the resulting change in yield strength can be estimated by [61], [62]:

(3)

$$\Delta\sigma_{cs} = M\alpha_{\varepsilon}(\varepsilon_c G)^{3/2}\left(\frac{2rf}{Gb}\right)^{1/2}$$

where α_ε is a constant (2.6), ε_c is the constrained lattice misfit, $\varepsilon_c = (2/3)\Delta a/a$. Modulus mismatch strengthening (σ_{ms}) arises due to difference between the shear modulus of the matrix and coherent phases, and the due change in yield strength can be expressed by [61], [62]:

(4)

$$\Delta\sigma_{ms} = 0.0055M\Delta G^{3/2}\left(\frac{2f}{G}\right)^{1/2}\left(\frac{r}{b}\right)^{\frac{3m}{2}-1}$$

where ΔG is the difference in the shear moduli of Al and precipitate, and m is a constant (0.85). Ordering strengthening (σ_{os})) is associated with an energy increase required for moving dislocation to shear the precipitate, and is described by [61], [62]:

(5)

$$\Delta\sigma_{os} = 0.81M\left(\frac{\gamma_{APB}}{2b}\right)\left(\frac{3\pi f}{8}\right)^{1/2}$$

where γ_{APB} is the antiphase boundary energy of the interface between Al and precipitates, which was estimated to be 0.445 and 0.260 for Al_3Zr [20] and Mg_2Si [63], respectively.

Contribution from the precipitation strengthening is typically estimated by the minimum value of $\Delta\sigma_{orowan}$, $\Delta\sigma_{cs} + \Delta\sigma_{ms}$, and $\Delta\sigma_{os}$ [64]. At smaller radii, ordering strengthening mechanism dominates, while at larger radii, Orowan mechanism dominates. For the composition of the alloy fabricated at the laser power of 350 W and 1400 mm/s, the maximum volume fraction of the Al_3Zr and Mg_2Si was estimated to be 0.015 and 0.012 according to equilibrium phase diagrams (i.e., Al-Zr and Al-Mg_2Si). Amount of Mg in the as-built alloy (~0.8 wt%) was lower than the nominal 1 wt% Mg in AA6061, and some Si would have been consumed by the formation of $Al_{19}Fe_4MnSi_2$ phase: these would yield lower fraction of Mg_2Si. The as-built Zr-modified AA6061 contained the Al_3Zr phase as the primary solidification phase (i.e., grain refinement) and as precipitates developed by T6 heat treatment as shown in Fig. 10(b). In addition, an ideal heat-treatment for the aging of Al_3Zr should have been 400 °C or lower for 1–10 h. Therefore heat treatment at 500 °C to completely solutionize Mg_2Si would reduce the strengthening contribution by Al_3Zr. Therefore, in this estimation, a 50% reduction in the precipitation strengthening by both the Al_3Zr and Mg_2Si was considered.

Fig. 17 shows the estimated precipitation strengthening contributions from the Al_3Zr and Mg_2Si phases. Maximum possible increase in strengthening would be 175 MPa for 1–3 nm radii Al_3Zr precipitates, and 60 MPa for 1–15 nm radii Mg_2Si precipitates. Tzeng [65] examined the microstructure of as-cast Zr-modified AA6061 alloy after similar T6 heat treatment, and reported the radii of Mg_2Si needles as 3–5 nm and Al_3Zr precipitates as 4–8 nm. Therefore based on radii measurements, Mg_2Si and Al_3Zr precipitates would mainly contribute by ordering and Orowan mechanisms, respectively [66]. By using the similar radii of Mg_2Si and Al_3Zr, the overall increase in yield stress ($\Delta\sigma_y$) would be 140–185 MPa. However the increase in σ_y after T6 heat treatment was only 90 MPa as reported in Table 4.

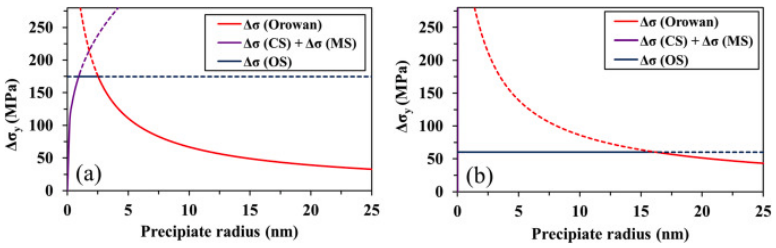

Fig. 17. Estimated contributions from various precipitation strengthening mechanisms on the increase in yield strength as a function of (a) Al_3Zr and (b) Mg_2Si precipitate radius.

Experimentally observed $\Delta\sigma_y$ after T6 heat treatment was significantly lower than that estimated by the theoretical models for Zr-modified AA6061. This may be due to a substantial reduction in the dislocation

density after T6 heat treatment. Dislocation density (ρ) can be measured using Dunn and Koch equation given by [67]:

(6)

$$\rho = \frac{\beta_{hkl}^2}{kb^2}$$

where β_{hkl} is the full-width at half maxima (FWHM) of the XRD peak, b is the burgers vector and k is the constant ($2\pi\ln 2$ for metals). The dislocation density in as-built and T6 heat treated LPBF AA6061 was estimated to be 10^{13} m^{-2} and 10^{12} m^{-2}, respectively, from the XRD patterns presented in Fig. 3. The T6 heat treatment lowered the dislocation density by approximately an order of magnitude in Zr-modified AA6061. Therefore, an optimization of heat-treatment to maximize the precipitation strengthening in LPBF Zr-modified AA6061 would be of interest for future studies.

5. Conclusions

Printability/buildability of unmodified AA6061 and modified AA6061 with 1 wt% Zr was examined as functions of LPBF laser power (200 and 350 W) and scan speed (100~1800 mm/s) using gas atomized alloy powders. The microstructure of unmodified AA6061 exhibited significant cracking and flaw formation at all LPBF parameters. Minor addition of 1 wt% Zr in AA6061 eliminated the cracking and substantially reduced the porosity so that the LPBF can be employed to additively manufacture Zr-modified AA6061 alloys. A laser power of 350 W, scan speed of 1400 mm/s, hatch spacing of 130 μm and slice thickness of 30 μm was identified as optimum LPBF parameter for Zr-modified AA6061 with the highest relative density greater than 99.7%.

Microstructure of unmodified AA6061 made by LPBF exhibited large columnar grains with <001> orientation in the build direction, which were also parallel to the intergranular cracks. However, Zr-modified AA6061 consisted of fine equiaxed grains along the melt-pool boundaries and the small columnar grains within individual melt pools. The addition of Zr resulted in primary solidification of fine Al_3Zr particles that acted as a heterogeneous nucleation sites, particularly at the melt-pool boundaries and promoted the formation of fine grains. This inhibited the epitaxial growth of large columnar grains and cracks found in unmodified LPBF AA6061. Tensile properties of dense, Zr-modified AA6061 produced by LPBF were superior to annealed or as-cast AA6061. Subsequent T6 heat treatment of LPBF Zr-modified AA6061 further improved the tensile properties with precipitation strengthening by Mg_2Si and Al_3Zr phases, which were also superior to the T6 heat treated wrought AA6061.

CRediT authorship contribution statement

Abhishek Mehta: Methodology, Validation, Formal analysis, Investigation, Data curation, Writing - original draft, Writing - review & editing. **Le Zhou**: Conceptualization, Methodology, Validation. **Thinh Huynh**: Investigation (gas atomization). **Sharon Park**: Investigation (gas atomization). **Holden Hyer**: Investigation (LPBF); Validation. **Shutao Song**: Investigation (mechanical testing) and Formal analysis. **Yuanli Bai**: Investigation (mechanical testing) and Formal analysis. **D. Devin Imholte**: Conceptualization, Resources, Writing - review & editing. **Nicolas E. Woolstenhulme**: Conceptualization, Resources, Writing - review & editing, Project administration, Funding acquisition. **Daniel M. Wachs**: Conceptualization, Resources, Writing - review & editing, Project administration, Funding acquisition. **Yongho Sohn**: Conceptualization, Methodology, Supervision, Writing - review & editing, Project administration, Funding acquisition.

Declaration of Competing Interest

The authors declare that they have no known competing financial interests or personal relationships that could have appeared to influence the work reported in this paper.

Acknowledgements

This research was sponsored by the Battelle Energy Alliances, LLC, under a contract, No. DE-AC07-05ID14517-214376 with collaboration from authors of Idaho National Laboratory. The views, opinions and conclusions made in this document are those of the authors and should not be interpreted as representing the official policies, either expressed or implied, of the Battelle Energy Alliances or Idaho National Laboratory or the U.S. Government. The U.S. Government is authorized to reproduce and distribute reprints for Government purposes notwithstanding any copyright notation herein.

References

[1] A. Lakshminarayanan, V. Balasubramanian, K. Elangovan. **Effect of welding processes on tensile properties of AA6061 aluminium alloy joints.** Int. J. Adv. Manuf. Technol., 40 (3–4) (2009), pp. 286-296, 10.1007/s00170-007-1325-0

[2] A. Mehta, N. Eriksson, R. Newell, L. Zhou, E. Schulz, W. Sprowes, F. Betancor, Y. Park, D.D. Keiser, Y.H. Sohn. **Phase transformations and microstructural development in the U-10 wt Pct Mo alloy with varying Zr Contents after heat treatments relevant to the monolithic fuel plate fabrication process.** Metall. Mater. Trans. A, 50 (1) (2019), pp. 72-96, 10.1007/s11661-018-4987-3

[3] A. Mehta, L. Zhou, E.A. Schulz, D.D. Keiser, J.I. Cole, Y.H. Sohn. **Microstructural characterization of AA6061 versus AA6061 HIP bonded cladding–cladding interface.** J. Phase Equilib. Diffus., 39 (2) (2018), pp. 246-254, 10.1007/s11669-018-0629-0

[4] R. Newell, A. Mehta, Y. Park, D. Keiser Jr., J. Cole, Y.H. Sohn. **Microstructural characteristics of plasma sprayed, electroplated, and co-rolled Zr diffusion barriers in hot isostatic pressed low enriched U-10 wt% Mo monolithic fuel plates.** J. Nucl. Mater., 523 (2019), pp. 91-100, 10.1016/j.jnucmat.2019.05.056

[5] R. Newell, A. Mehta, Y.J. Park, D.D. Keiser Jr., Y.H. Sohn. **Interdiffusion, reactions, and phase transformations observed during fabrication of low enriched uranium monolithic fuel system for research and test reactors.** Defect Diffus. Forum, 383 (2018), pp. 10-16, 10.4028/www.scientific.net/DDF.383.10

[6] R. Newell, A. Mehta, Y.J. Park, Y.H. Sohn, J.F. Jue, D.D. Keiser Jr. **Relating diffusion couple experiment results to observed as-fabricated microstructures in low-enriched U-10wt% Mo monolithic fuel plates.** Defect Diffus. Forum, 375 (2017), pp. 18-28, 10.4028/www.scientific.net/DDF.375.18

[7] A. Mehta, J. Dickson, R. Newell, D.D. Keiser, Y. Sohn. **Interdiffusion and reaction between Al and Zr in the temperature range of 425 to 475 °C.** J. Phase Equilib. Diffus., 40 (4) (2019), pp. 482-494, 10.1007/s11669-019-00729-9

[8] A. Mehta, L. Zhou, D.D. Keiser Jr., Y. Sohn. **Anomalous growth of Al_8Mo_3 phase during interdiffusion and reaction between Al and Mo.** J. Nucl. Mater., 539 (2020), Article 152337, 10.1016/j.jnucmat.2020.152337

[9] Y. Park, R. Newell, A. Mehta, D. Keiser Jr., Y. Sohn. **Interdiffusion and reaction between U and Zr.** J. Nucl. Mater., 502 (2018), pp. 42-50, 10.1016/j.jnucmat.2018.01.063

[10] S. Kou. **A simple index for predicting the susceptibility to solidification cracking.** Weld. J., 94 (2015), pp. 374-388

[11] N.T. Aboulkhair, M. Simonelli, L. Parry, I. Ashcroft, C. Tuck, R. Hague. **3D printing of aluminium alloys: additive manufacturing of aluminium alloys using selective laser melting.** Prog. Mater. Sci., 106 (2019), Article 100578, 10.1016/j.pmatsci.2019.100578

[12] E. Louvis, P. Fox, C.J. Sutcliffe. **Selective laser melting of aluminium components.** J. Mater. Process. Technol., 211 (2) (2011), pp. 275-284, 10.1016/j.jmatprotec.2010.09.019 (2011)

[13] L. Zhou, A. Mehta, E. Schulz, B. McWilliams, K. Cho, Y.H. Sohn. **Microstructure, precipitates and hardness of selectively laser melted AlSi10Mg alloy before and after heat treatment.** Mater. Charact., 143 (2018), pp. 5-17, 10.1016/j.matchar.2018.04.022

[14] M. Zavala-Arredondo, T. London, M. Allen, T. Maccio, S. Ward, D. Griffiths, A. Allison, P. Goodwin, C. Hauser. **Use of power factor and specific point energy as design parameters in laser powder-bed-fusion (L-PBF) of AlSi10Mg alloy.** Mater. Des., 182 (2019), Article 108018, 10.1016/j.matdes.2019.108018

[15] K.G. Prashanth, S. Scudino, J. Eckert. **Defining the tensile properties of Al-12Si parts produced by selective laser melting.** Acta Mater., 126 (2017), pp. 25-35, 10.1016/j.actamat.2016.12.044

[16] X. Li, X. Wang, M. Saunders, A. Suvorova, L. Zhang, Y. Liu, M. Fang, Z. Huang, T.B. Sercombe. **A selective laser melting and solution heat treatment refined Al–12Si alloy with a controllable ultrafine eutectic microstructure and 25% tensile ductility.** Acta Mater., 95 (2015), pp. 74-82, 10.1016/j.actamat.2015.05.017

[17] H. Hyer, L. Zhou, A. Mehta, Y.H. Sohn. **Effects of alloy composition and solid-state diffusion kinetics on powder bed fusion cracking susceptibility.** J. Phase Equilib. Diffus. (2020), 10.1007/s11669-020-00844-y

[18] S.C. Chou, M. Trask, J. Danovitch, X.L. Wang, J.P. Choi, M. Brochu. **Pulsed laser powder bed fusion additive manufacturing of A356.** Mater. Charact., 143 (2018), pp. 27-33, 10.1016/j.matchar.2018.02.004

[19] L. Zhou, T. Huynh, S. Park, H. Hyer, A. Mehta, S. Song, Y. Bai, B. McWilliams, K. Cho, Y.H. Sohn. **Laser powder bed fusion of Al–10 wt% Ce alloys: microstructure and tensile property.** J. Mater. Sci., 55 (29) (2020), pp. 14611-14625, 10.1007/s10853-020-05037-z

[20] L. Zhou, H. Hyer, S. Park, H. Pan, Y. Bai, K.P. Rice, Y.H. Sohn. **Microstructure and mechanical properties of Zr-modified aluminum alloy 5083 manufactured by laser powder bed fusion.** Addit. Manuf., 28 (2019), pp. 485-496, 10.1016/j.addma.2019.05.027

[21] B.A. Fulcher, D.K. Leigh, T.J. Watt, Comparison of AlSi10Mg and Al 6061 processed through DMLS, in: Proceedings of the Solid Freeform Fabrication (SFF) Symposium, Austin, TX, USA, (2014).

[22] N. Kaufmann, M. Imran, T.M. Wischeropp, C. Emmelmann, S. Siddique, F. Walther. **Influence of process parameters on the quality of aluminium alloy EN AW 7075 using Selective Laser Melting (SLM).** Phys. Procedia, 83 (2016), pp. 918-926, 10.1016/j.phpro.2016.08.096

[23] B. Ahuja, M. Karg, K.Y. Nagulin, M. Schmidt. **Fabrication and characterization of high strength Al-Cu alloys processed using laser beam melting in metal powder bed.** Phys. Procedia, 56 (2014), pp. 135-146, 10.1016/j.phpro.2014.08.156

[24] A. Sonawane, G. Roux, J.-J. Blandin, A. Despres, G. Martin. **Cracking mechanism and its sensitivity to processing conditions during laser powder bed fusion of a structural aluminum alloy.** Materialia, 15 (2021), Article 100976, 10.1016/j.mtla.2020.100976

[25] L. Loh, Z. Liu, D. Zhang, M. Mapar, S. Sing, C. Chua, W. Yeong. **Selective Laser Melting of aluminium alloy using a uniform beam profile.** Virtual Phys. Prototyp., 9 (1) (2014), pp. 11-16, 10.1080/17452759.2013.869608

[26] J.H. Martin, B.D. Yahata, J.M. Hundley, J.A. Mayer, T.A. Schaedler, T.M. Pollock. **3D printing of high-strength aluminium alloys.** Nature, 549 (2017), pp. 365-369, 10.1038/nature23894

[27] M. Opprecht, J.-P. Garandet, G. Roux, C. Flament, M. Soulier. **A solution to the hot cracking problem for aluminium alloys manufactured by laser beam melting.** Acta Mater., 197 (2020), pp. 40-53, 10.1016/j.actamat.2020.07.015

[28] N. Qbau, N. Nam, N. Ca, N. Hien. **The crack healing effect of scandium in aluminum alloys during laser additive manufacturing.** J. Manuf. Process., 50 (2020), pp. 241-246, 10.1016/j.jmapro.2019.12.050

[29] S.Z. Uddin, L.E. Murr, C.A. Terrazas, P. Morton, D.A. Roberson, R.B. Wicker. **Processing and characterization of crack-free aluminum 6061 using high-temperature heating in laser powder bed fusion additive manufacturing.** Addit. Manuf., 22 (2018), pp. 405-415, 10.1016/j.addma.2018.05.047

[30] A.H. Maamoun, Y.F. Xue, M.A. Elbestawi, S.C. Veldhuis. **The effect of selective laser melting process parameters on the microstructure and mechanical properties of Al6061 and AlSi10Mg alloys.** Materials, 12 (1) (2019), p. 12, 10.3390/ma12010012

[31] S.Z. Uddin, D. Espalin, J. Mireles, P. Morton, C. Terrazas, S. Collins, L.E. Murr, R. Wicker, Laser powder bed fusion fabrication and characterization of crack-free aluminum alloy 6061 using in-process powder bed induction heating, in: Proceedings of the SFF symposium, (2017) 214–227.

[32] W.C. Oliver, G.M. Pharr. **An improved technique for determining hardness and elastic modulus using load and displacement sensing indentation experiments.** J. Mater. Res., 7 (6) (1992), pp. 1564-1583, 10.1557/JMR.1992.1564

[33] W.C. Oliver, G.M. Pharr. **Measurement of hardness and elastic modulus by instrumented indentation: advances in understanding and refinements to methodology.** J. Mater. Res., 19 (1) (2004), pp. 3-20, 10.1557/jmr.2004.19.1.3

[34] L. Zhou, A. Mehta, B. McWilliams, K. Cho, Y.H. Sohn. **Microstructure, precipitates and mechanical properties of powder bed fused inconel 718 before and after heat treatment.** J. Mater. Sci. Technol., 35 (6) (2019), pp. 1153-1164, 10.1016/j.jmst.2018.12.006

[35] T. Qi, H. Zhu, H. Zhang, J. Yin, L. Ke, X. Zeng. **Selective laser melting of Al7050 powder: melting mode transition and comparison of the characteristics between the keyhole and conduction mode.** Mater. Des., 135 (2017), pp. 257-266, 10.1016/j.matdes.2017.09.014

[36] C. Alcock, V. Itkin, M. Horrigan. **Vapour pressure equations for the metallic elements: 298–2500 K.** Can. Metall. Q., 23 (3) (1984), pp. 309-313, 10.1179/cmq.1984.23.3.309

[37] H. Hyer, L. Zhou, G. Benson, B. McWilliams, K. Cho, Y.H. Sohn. **Additive manufacturing of dense WE43 Mg alloy by laser powder bed fusion.** Addit. Manuf., 33 (2020), Article 101123, 10.1016/j.addma.2020.101123

[38] W.E. King, H.D. Barth, V.M. Castillo, G.F. Gallegos, J.W. Gibbs, D.E. Hahn, C. Kamath, A.M. Rubenchik. **Observation of keyhole-mode laser melting in laser powder-bed fusion additive manufacturing.** J. Mater. Process. Technol., 214 (12) (2014), pp. 2915-2925, 10.1016/j.jmatprotec.2014.06.005

[39] T. Larimian, M. Kannan, D. Grzesiak, B. AlMangour, T. Borkar. **Effect of energy density and scanning strategy on densification, microstructure and mechanical properties of 316L stainless steel processed via selective laser melting.** Mater. Sci. Eng. A, 770 (2020), Article 138455, 10.1016/j.msea.2019.138455

[40] M.J. Cieslak, P.W. Fuerschbach. **On the weldability, composition, and hardness of pulsed and continuous Nd:YAG laser welds in aluminum alloys 6061, 5456, and 5086.** Metall. Trans. B, 19 (2) (1988), pp. 319-329, 10.1007/BF02654217

[41] J. Zhang, Z. Fan, Y. Wang, B. Zhou. **Equilibrium pseudobinary Al–Mg2Si phase diagram.** Mater. Sci. Technol., 17 (5) (2001), pp. 494-496, 10.1179/026708301101510311

[42] K.E. Knipling, D.C. Dunand, D.N. Seidman. **Nucleation and precipitation strengthening in dilute Al-Ti and Al-Zr alloys.** Metall. Mater. Trans. A, 38 (10) (2007), pp. 2552-2563, 10.1007/s11661-007-9283-6 (2007)

[43] L. Wang, X. Jiang, Y. Zhu, Z. Ding, X. Zhu, J. Sun, B. Yan. **Investigation of performance and residual stress generation of AlSi10Mg processed by selective laser melting.** Adv. Mater. Sci. Eng., 2018 (2018), Article 7814039, 10.1155/2018/7814039

[44] ASM Handbook. **Properties and Selection: Nonferrous Alloys and Special-Purpose Materials.** ASM Handbook, ASM international ed. (1990), p. 3470

[45] W. Qin, J. Li, Y. Liu, J. Kang, L. Zhu, D. Shu, P. Peng, D. She, D. Meng, Y. Li. **Effects of grain size on tensile property and fracture morphology of 316L stainless steel.** Mater. Lett., 254 (2019), pp. 116-119, 10.1016/j.matlet.2019.07.058

[46] H. Hyer, L. Zhou, A. Mehta, S. Park, T. Huynh, S. Song, Y. Bai, K. Cho, B. McWilliams, Y.H. Sohn. **Composition-dependent solidification cracking of aluminum-silicon alloys during laser powder bed fusion.** Acta Mater., 208 (2021), Article 116698, 10.1016/j.actamat.2021.116698
[47] I. Novikov. **Hot cracking of nonferrous metals and alloys, ed.** Nauka, Moscow (1966)
[48] M.C. Flemings. Solidification Processing, McGraw-Hill, New York (1974)
[49] W. Kurz, D.J. Fisher. Fundamentals of Solidification (4th ed.), Trans Tech Publ (1989)
[50] C. Gourlay, A. Dahle. **Dilatant shear bands in solidifying metals.** Nature, 445 (2007), pp. 70-73, 10.1038/nature05426
[51] S. Kou. **A criterion for cracking during solidification.** Acta Mater., 88 (2015), pp. 366-374, 10.1016/j.actamat.2015.01.034
[52] J. Liu, S. Kou. **Crack susceptibility of binary aluminum alloys during solidification.** Acta Mater., 110 (2016), pp. 84-94, 10.1016/j.actamat.2016.03.030
[53] J. Liu, S. Kou. **Effect of diffusion on susceptibility to cracking during solidification.** Acta Mater., 100 (2015), pp. 359-368, 10.1016/j.actamat.2015.08.064
[54] B. Sundman, I. Ansara. **The Gulliver–Scheil method for the calculation of solidification paths.** The SGTE Casebook (Second Ed.), Elsevier (2008), pp. 343-346, 10.1533/9781845693954.3.343
[55] X. Nie, H. Zhang, H. Zhu, Z. Hu, L. Ke, X. Zeng. **Effect of Zr content on formability, microstructure and mechanical properties of selective laser melted Zr modified Al-4.24 Cu-1.97 Mg-0.56 Mn alloys.** J. Alloy. Compd., 764 (2018), pp. 977-986, 10.1016/j.jallcom.2018.06.032
[56] K. Nogi. **The role of wettability in metal–ceramic joining.** Scr. Mater., 62 (12) (2010), pp. 945-948, 10.1016/j.scriptamat.2010.03.007
[57] D. Gu, Y.C. Hagedorn, W. Meiners, G. Meng, R.J.S. Batista, K. Wissenbach, R. Poprawe. **Densification behavior, microstructure evolution, and wear performance of selective laser melting processed commercially pure titanium.** Acta Mater., 60 (9) (2012), pp. 3849-3860, 10.1016/j.actamat.2012.04.006
[58] H. Okamoto. **Al-Zr (aluminum-zirconium).** J. Phase Equilib., 23 (5) (2007), pp. 455-456, 10.1361/105497102770331497
[59] J.A. Glerum, C. Kenel, T. Sun, D.C. Dunand. **Synthesis of precipitation-strengthened Al-Sc, Al-Zr and Al-Sc-Zr alloys via selective laser melting of elemental powder blends.** Addit. Manuf., 36 (2020), Article 101461, 10.1016/j.addma.2020.101461
[60] S. Griffiths, M. Rossell, J. Croteau, N.Q. Vo, D.C. Dunand, C. Leinenbach. **Effect of laser rescanning on the grain microstructure of a selective laser melted Al-Mg-Zr alloy.** Mater. Charact., 143 (2018), pp. 34-42, 10.1016/j.matchar.2018.03.033 (2018)
[61] K. Ma, H. Wen, T. Hu, T.D. Topping, D. Isheim, D.N. Seidman, E.J. Lavernia, J.M. Schoenung. **Mechanical behavior and strengthening mechanisms in ultrafine grain precipitation-strengthened aluminum alloy.** Acta Mater., 62 (2014), pp. 141-155, 10.1016/j.actamat.2013.09.042
[62] H. Wen, T.D. Topping, D. Isheim, D.N. Seidman, E.J. Lavernia. **Strengthening mechanisms in a high-strength bulk nanostructured Cu–Zn–Al alloy processed via cryomilling and spark plasma sintering.** Acta Mater., 61 (8) (2013), pp. 2769-2782, 10.1016/j.actamat.2012.09.036
[63] O. Myhr, Ø. Grong, S. Andersen. **Modelling of the age hardening behaviour of Al–Mg–Si alloys.** Acta Mater., 49 (1) (2001), pp. 65-75, 10.1016/S1359-6454(00)00301-3
[64] K.E. Knipling, R.A. Karnesky, C.P. Lee, D.C. Dunand, D.N. Seidman. **Precipitation evolution in Al–0.1Sc, Al–0.1Zr and Al–0.1Sc–0.1Zr (at%) alloys during isochronal aging.** Acta Mater., 58 (15) (2010), pp. 5184-5195, 10.1016/j.actamat.2010.05.054
[65] Y.C. Tzeng. **Effects of Zr on the microstructure and mechanical properties of 6061 alloys.** Mater. Sci. Forum, 917 (2018), pp. 202-206, 10.4028/www.scientific.net/MSF.917.202

[66] R. Li, M. Wang, Z. Li, P. Cao, T. Yuan, H. Zhu. **Developing a high-strength Al-Mg-Si-Sc-Zr alloy for selective laser melting: crack-inhibiting and multiple strengthening mechanisms.** Acta Mater., 193 (2020), pp. 83-98, 10.1016/j.actamat.2020.03.060

[67] C. Dunn, E. Koch. **Comparison of dislocation densities of primary and secondary recrystallization grains of Si-Fe.** Acta Metall., 5 (10) (1957), pp. 548-554, 10.1016/0001-6160(57)90122-0